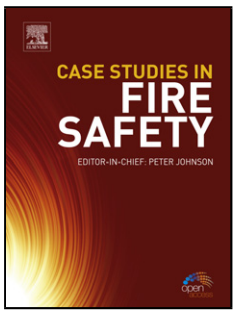

Title: The galvanic corrosion of welded ultra-high strength steels used for automotive applications

Authors: N. Wint, J. Leung, J.H. Sullivan, D.J. Penney, Y. Gao

PII: S0010-938X(17)32167-4
DOI: https://doi.org/10.1016/j.corsci.2018.03.025
Reference: CS 7441

To appear in:

Received date: 7-12-2017
Revised date: 14-3-2018
Accepted date: 15-3-2018

Please cite this article as: Wint N, Leung J, Sullivan JH, Penney DJ, Gao Y, The galvanic corrosion of welded ultra-high strength steels used for automotive applications, *Corrosion Science* (2010), https://doi.org/10.1016/j.corsci.2018.03.025

The galvanic corrosion of welded ultra-high strength steels used for automotive applications

N. Wint [a,*], J. Leung [a], J.H. Sullivan [a], D. J. Penney [a], Y. Gao [b]

[a] *Materials Research Centre, College of Engineering, Swansea University, Bay Campus, Fabian Way, Crymlyn Burrow, Swansea, UK, SA1 8EN*

[b] *Product Engineering, Tata Steel UK*

*Corresponding author: Tel: +44 7376357305
E-mail address: n.wint@swansea.ac.uk

Abstract: In situ Scanning Vibrating Electrode Technique and time lapse photography were used to study the galvanic corrosion of high strength low alloy (HSLA) steel, laser welded to hot stamped ultra high strength steel (UHSS) in 0.017 M NaCl. Samples of HSLA welded to UHSS exhibited corrosion focused on the UHSS. This galvanic effect was due to a -0.2 V vs. SHE difference in OCP for the UHSS. SVET derived metal loss increased by a factor of >2 for this couple. The localised corrosion observed may reduce the fatigue resistance and is of significance considering the increased use of thinner UHSS.

Keywords; A Steel

1. Introduction

As part of its commitment to the Kyoto Protocol [1], the European Union have issued legislation which dictates that the CO_2 emissions from 95 % of each manufacturer's fleet of new cars must be reduced to 95 $g.km^{-1}$ by 2020, this increasing to 100 % by 2021 [2].

One way in which this can be achieved is by using sheet steel components of thinner gauge, which resultantly weigh less and thus require less fuel throughout the in service life.

State-of-the-art car bodies and chassis and suspension (C&S) steel components, for which heavy gauge steel is commonly used [3], contribute a weight share of 60 to 80% [4] of the total vehicle weight and therefore provide an opportunity for weight reduction.

The use of ultra-high strength steels (UHSS), which allow for the retention of strength whilst reducing gauge, is consequently increasing [4-7]. However, down gauging raises corrosion concerns, this being especially true of the C&S components which are subject to harsh environmental cycling, and are typically uncoated due to cost considerations and technological limitations with respect to coating integrity at high temperatures [8-10]. Furthermore, components are commonly welded together, introducing further complications [10-13]. The welding process induces a variety of microstructures within the steel components as well as geometrical and chemical differences that can influence the severity of corrosion [10-11].

UHSS grades are defined as having a yield strength in excess of 550 MPa and tensile strengths of over 700 MPa [13-14]. Their strength is generally attributed to solid solution or precipitation hardening. This modifies the material's chemistry, grain size, phase distribution and response to work hardening [13-14]. One such high strength steel that is being

22MnB5. Once heat treated, boron steels are fully martensitic with a typical tensile strength of 1500 MPa [7]. Characteristic properties are high hardness, high stiffness and high tensile strength [7]. In comparison, high strength, low alloy steel grades (HSLA), which typically gain strength from precipitation hardening and grain refinement are typically used for C&S components due to their combination of both high strength and relatively high formability [15-17]. Due to the difference in both chemistry and microstructure, the coupling of these two steel products via welding may result in increased susceptibility to localised galvanic corrosion.

Chassis components belong to the category of safety components meaning they must never fail [18] and consequently the corrosion performance of UHSS grades typically used during down gauging is of significant interest.

Previous research into the corrosion of welded 22MnB5 has shown that the weld metal possessed less corrosion resistance than the base metal [10]. This finding was attributed to the microstructure variation of the weld metal [10]. Similarly, electrochemical studies were used to conclude that welded 22MnB5 is more susceptible to pitting than the un-welded material [11]. However, there has been little work into the corrosion of UHSS coupled to HSLA grades.

Here, a combination of electrochemistry, the scanning vibrating electrode technique (SVET), and time lapse microscopy is used to study the galvanic corrosion of a HSLA steel, typically used during the production of automotive components, laser welded to a UHSS hot stamped boron grade. The SVET technique allows for the measurement of spatially resolved net current density values and subsequently offers scope to study galvanic

corrosion [19-20] and has previously been used to study the cut edge corrosion of Zn coated steels [21-23].

2. Materials and Methods

NaCl, and all other chemicals were obtained from Sigma Aldrich Chemical Co. and were of analytical grade purity. A 0.017 mol.L^{-1} (M) NaCl (aq) electrolyte was used throughout.

Both steel grades were supplied by Tata Steel UK. The HSLA grade consisted of ferrite-pearlite microstructure. The gauge of the samples was 3 mm and the chemical composition is shown in Table 1 and is typical of the grade, conforming to Uncoated (EN10149-2:2013): S315MCBS.

(Table 1)

The pre-heat treatment UHSS grade consisted of a ferrite-pearlite microstructure which is achieved through a combination of boron addition and a simulated die-quenching process. The gauge of the samples was 2.8 mm and the chemical composition is shown in Table 2 and is typical of the grade, which conforms to Uncoated (EN10083-3:2006):22MnB5.

(Table 2)

Boron steels are manufactured from casts to strip via hot rolling and cooled on the run out table to produce the ferritic pearlitic microstructure. The steel was developed to be produced in this ferritic pearlitic 'as received' (AR) condition rather than fully martensitic to avoid wear issues during subsequent processing and tooling [24]. The diffusionless transformation from austenite to martensite is achieved through a combination of boron additions and a hot stamping process. Samples used during this work were primarily in the

heat treated (HT), martensitic state as opposed to AR, in order to best replicate in service conditions.

To achieve this transformation AR 22MnB5 samples were placed onto a perforated iron rack inside Thermo Scientific Thermolyne for 5 minutes at 900°C. Upon removal from the furnace samples were immediately submerged into water to rapidly cool and force the diffusionless transformation from austenite to martensite. During the heat treatment cycle the temperature of the samples were recorded using a welded k type thermocouple and logged through an Omega OM-DAQ-USB 2401 data logger.

The steel grades were welded together using light amplification by stimulated emission of radiation (LASER) welding. using a Remote Laser Welding Robot 'Comau Smartlaser' at Warwick Manufacturing Group (WMG) situated in The University of Warwick. Three different variants were produced; HSLA-HSLA, HT UHSS- HT UHSS, HSLA- HT UHSS. Laser welding was chosen due to the reduced size of the heat affected zone (HAZ) and therefore the subsequent decrease in the induced microstructural and chemical properties changes associated, when compared to other welding techniques [11-12]. In addition, laser welding requires no filler wire and hence removes the complication of additional elements, such as copper, becoming entrained in the weld zone, this in turn influencing electrochemical behaviour.

For microstructural analysis samples were mounted in a conductive compound and ground and polished to a 1μm finish using a water based diamond suspension. A 2 % nital etchant was used to reveal the microstructures of the steels. Optical images were captured by a Reichert JUNG MeF3 light optical microscope with a Nikon DSFi1 camera. Scanning electron microscopy (SEM) images were acquired using a JEOL JSM 6100 SEM.

In the case of electrochemical characterisation experiments, coupons of approximately 40 mm x 30 mm were cut from large sheet. Samples were ground to a European P-grade P1200 grit finish using silicon carbide (SiC) abrasive paper and were cleaned and degreased using ethanol and distilled water before experimentation. For open circuit potential (OCP) measurements a 1 cm × 1 cm area of the sample was exposed using extruded Polytetrafluoroethylene (PTFE) tape (type 5490 HD supplied by 3 M). A Solartron 1280 Electrochemical Measurement Unit was used and potential values were recorded with respect to a saturated calomel electrode (SCE) reference electrode at 25 °C, and converted to values with respect to a standard hydrogen electrode (SHE). **A zero resistance ammeter was used to measure the galvanic current between the HSLA- HT UHSS couple at OCP.** Samples were prepared and taped using the same methodology as in the case of OCP measurements. The experimental setup was such that the 1 cm x 1 cm areas exposed on each sample were facing one another and at a distance of 1 cm apart. Both types of electrochemical measurement were made three times.

SVET scans were performed to give spatial mechanistic and time resolved insights into the galvanic corrosion occurring on welded material. The SVET makes use of the alternating potential arising from the oscillation of the microtip in the ohmic potential field that exists as a result of the ionic current in the electrolyte solution above a corroding surface.

References to the design of SVET instrumentation, operation and calibration to give values of current density along the axis of probe vibration **(i_z),** have been made elsewhere [19, 25-26]. In brief, a glass encased 125 μm diameter platinum wire microtip is vibrated, in the z direction, at a constant frequency (140 Hz), amplitude (25 μm) and height (100 μm) above the immersed corroding sample.

Welded samples were mounted in non-conducting acrylic resin so that the cross section was exposed. The samples were then ground to a European P-grade P1200 grit finish using silicon carbide (SiC) abrasive paper and polished using a water based 6 μm and 1 μm diamond suspension. Finally, a *ca* 2 x 0.5 cm area was isolated using insulating extruded PTFE self-adhesive tape so that only the area to be scanned was exposed.

The SVET probe made measurements along both the width and length of the sample, creating a mesh of data points. One scan was taken per hour for a period of 24 hours. Each scan took between 6.5 and 8 minutes, depending on sample size. The dissolved oxygen and carbon dioxide concentrations in bulk solution were 2.8 x 10^{-4} M and 1.32 x 10^{-5} M respectively, the equilibrium concentrations for air saturated water [27]. Three experiments were conducted for each couple.

The time dependent total anodic current (I_t) associated with each of the i_z distribution maps produced per scan, were calculated by numerical integration of all the anodic values of i_z (> 0) carried out over the entirety of the exposed surface using the trapezium rule, according to equation (1)

$$I_t = A.\, i_t = \int_0^X \int_0^Y [\, i_{z(x,y,t)} > 0]\, \mathrm{d}x\, \mathrm{d}y \qquad (1)$$

where A is the sample area, and x and y are the length and width of the SVET scan respectively and t is the time. This allowed one I_t value to be obtained for each scan. Dividing I_t by A gives an area averaged anodic current density value i_t. The total charge density emitted from the areas of local anodic activity over the duration of the experiments was thus calculated using equation (2) and the mass loss in g.cm^{-2} was determined using Faraday's Law and converted to units of μg.cm^{-2}.

$$q = \int_{t=0}^{t=t_{max}} i_t dt \quad (2)$$

where q is the charge density in C.cm^{-2} and t_{max} is the immersion period in seconds. It is assumed that i_t remains constant between scans.

It should be considered that current density was measured 100 μm above the metal surface and thus the current detection efficiency was dependent on the local anode-cathode spacing. I_t values were derived solely from localised corrosion and the contribution from general corrosion was not accounted for. SVET derived mass loss values are therefore minimum estimates and are treated as semi quantitative. Despite this, they are useful when making direct comparisons of mass loss from different samples, and values obtained previously have been found to correlate with long term external weathering Zn run off tests [28].

Samples for in situ time lapse microscopy were prepared in the same way as for SVET experiments but were also etched using a 2 % nital solution. The sample configuration was such that the initiation and progression of corrosion could be ascertained at a microstructural level associated with weld zones whilst also assessing any galvanic effects of dissimilar metal couples. Due to these samples being larger than the allocated 0.5 mm^2 that the microscope lens could observe, a 0.5 mm height rectangle was exposed using extruded PTFE self-adhesive tape across the welded materials, then images were taken along the length of this rectangle manually by moving the microscope stage at intervals of approximately two-minutes, as shown in Figure 1. These images were then stitched together using Adobe Photoshop to create one high resolution image of the exposed area. The rectangular exposed area height always remained the same at 0.5 mm, but the length and amount of images taken across the exposed area varied from sample to sample due to the differences in heat affected weld zones.

(Figure 1)

In situ time lapse optical microscopy, which allowed the imaging of immersed corroding samples at a microstructural level, was employed following a methodology developed previously [29-30]. A polycarbonate time-lapse cell was used. The time-lapse cell had an open side to which a mounted sample was secured via an inert adhesive. Once the time-lapse cell was secured onto the mounted sample it was carefully filled with the electrolyte via the entry points, drilled in at either side of the cell, using a syringe. These holes were then sealed for the remainder of the experiment. The top of the time-lapse cell was open and a 0.13-0.16 mm optical quality borosilicate Agar Scientific coverglass was secured using Loctite Double Bubble 2-Part Epoxy, assuring the cell was air and water tight. A Meiji MT8000 microscope was then manoeuvred so as to image the exposed sample area. Images were captured using an infinity 2 camera attachment.

3. Results

3.1 Materials Characterisation

The surface morphology of the steel grades was determined using SEM and optical microscopy. Figure 2a shows an optical image of the HSLA grade steel. The microstructure consists of a fine grained ferrite matrix, grain boundary iron carbides, and islands of pearlite, which is characterised by a lamellar structure consisting of alternate layers of ferrite and cementite [16]. Figure 2b shows an optical image of the HT UHSS. The microstructure is martensitic. In the accompanying SEM image the laths of martensite, which are formed within prior austenite grains, are visible.

(Figure 2)

The OCP of the steel grades in 0.017 M NaCl (aq) was measured at 25 °C, prior to welding, to determine electrochemical differences between the two steel grades, and are shown in Figure 3. Three measurements are shown to clarify that any differences in behaviour observed can be attributed to differences in steel grade, rather than data scatter from sample to sample. Measurements were made on the HSLA steel in the AR (in-service) condition and the UHSS in the AR and HT (in-service) condition in order to ascertain if the heat treatment affected the electrochemical properties of the steel. Initially the measured potential value is almost 0.2 V higher in the case of HSLA steel than that for both the AR and HT UHSS. However, after approximately 10 hours the potential associated with the HSLA sample falls by ca. 0.1 V. At the end of the 24 hour time period the potential values recorded are, within error, similar for both the UHSS and HSLA steel samples. A comparison of the AR and HT UHSS data showed that OCP values both dropped from initial potentials of -0.25 V vs. SHE to relatively stable OCP values of -0.43 V ± 0.05 V vs. SHE. However, this fall in potential was obtained in around 3 hours for the HT UHSS in comparison with 7 hours for the AR UHSS.

The galvanic current running from the HT UHSS (working electrode) to the HSLA steel at OCP was recorded as a function of time using a zero resistance ammeter and the results are shown in Figure 4. Three measurements are shown to differentiate between a variation resulting from steel grade and variation in samples of the same grade. The positive current indicates that the HT UHSS is acting anodically with respect to the HSLA steel sample when coupled galvanically. There is an initial rapid rise in current 60 $\mu A.cm^{-2}$ over the first 3 hours.

(Figure 3)

(Figure 4)

3.3 SVET Results

The SVET has been used to spatially map anodic and cathodic areas on laser welded steel couples. The couples of material investigated were HSLA-HSLA, HT UHSS- HT UHSS and HSLA- HT UHSS in order to ascertain the regions of preferred corrosion (if any) and the effect of galvanically coupling the two steel substrates when welded.

HSLA-HSLA; The SVET derived surface plots of the normal current density above the welded HSLA steel sample freely corroding in 0.017 M NaCl (aq) electrolyte are shown in Figure 5. The plots shown were obtained after varying times during the 24 hours of electrolyte immersion, and were chosen to best represent the mechanistic behaviour of the system. Areas of net anodic metal dissolution are shown in red, with areas of net cathodic activity in blue. After 1 hour of exposure to the electrolyte a number of low intensity anodic features of current density **< 100 µA.cm^{-2}** were observed at the top and bottom edges of the welded material. However, after 8 hours of immersion a definitive localised region of corrosion activity had developed that was coincident with the welded zone, with the base metal either side of the weld remaining generally cathodic. This region of anodic attack persisted for the remainder of the 24 hour experiment. The image of the sample post immersion shown in Figure 5 supports the findings of the SVET. A region of red rust was observed over the weld zone coincident with the localised anodic attack demonstrated by the SVET. The base HSLA metal outside of the weld zone was relatively unaffected by corrosion with little red rust observed beyond the weld zone. However, some darkening of the substrate to the left hand side of the weld zone was observed after 24 hours of immersion. It can, nonetheless, be concluded that the preferential site of attack in the

HSLA-HSLA couple was the weld zone.

(Figure 5)

HT UHSS- HT UHSS; Figure 6 shows the SVET derived surface plots of the normal current density above the welded HT UHSS sample freely corroding in 0.017 M NaCl (aq) electrolyte. After 1 hour localised anodic features were observed to initiate at the weld area, but were located at the periphery of the weld zone rather than the central area of the weld. After 8 hours these anodic features persisted and had grown into the central part of the weld zone. Initiation of further localised anodic features was also observed associated with the base substrate away from the weld area. Between 16 and 24 hours the anodic features at the weld had reduced in intensity and further anodic activity was observed on the base substrate away from the weld zone. An image of the sample post immersion is also shown in Figure 6 and shows significant red rusting associated with the weld area and also dark, spot like, localised corrosion features on the substrate away from the weld area (circled in Figure 6), this supporting the SVET findings.

(Figure 6)

HSLA- HT UHSS; The SVET derived surface plots of the normal current density above the HSLA steel sample welded to the HT UHSS, freely corroding in 0.017 M NaCl (aq) electrolyte are shown in Figure 7. During the first hour of immersion localised anodic activity once again initiates at the weld between the two materials with initiation occurring preferentially on the side of the weld zone associated with the HT UHSS. Whilst anodic activity is localised to the weld region after 1 hour of immersion, thereafter corrosion attack spreads across the HT UHSS, whilst the HSLA steel remains completely cathodic

The presence of corrosion product can be seen over the weld zone and the HT UHSS surface post immersion, whereas the HSLA substrate remains relatively visually unscathed. This behaviour was observed in the case of repeat measurements.

The total SVET derived mass loss for the three welded steel configurations were calculated using Equation 2 and are shown in Table 3 in µg.cm^{-2}, following conversion. The confidence limits (errors) shown relate to one standard deviation on the mean, on the basis of three measurements. The mass loss from welded HSLA-HSLA **(241 µg.cm^{-2})** and welded HT UHSS-HT UHSS **(197 µg.cm^{-2})** is somewhat similar, but approximately doubles in the case that the dissimilar grades HSLA- HT UHSS **(505 µg.cm^{-2})** are welded to one another, indicative of a galvanic acceleration due to the coupling of the two dissimilar substrates.

(Figure 7)

(Table 3)

3.4 Time Lapse Microscopy Results

Time lapse microscopy experiments were conducted for all three combinations of welded samples, as with SVET in 3.3. This technique allows the microstructure to be fully observed during testing and thus the extent of the weld and the heat affected zones (HAZ) to be established. Thus, on immersion the location of the preferential corrosion initiation and growth within these differences in microstructure may be evaluated.

Figures 8 A-F shows the surface of welded HSLA-HSLA steel samples at ca. 2 minute intervals. Initially several anodes appear in the welded zone and associated corrosion product rings are formed. The presence of rings of corrosion product, previously suggested

to form at the boundary of ionic counter currents from radial diffusion of metal ions from the anodic site and migration of hydroxide ions from the cathodic regions, [31] indicate that the corrosion occurring is primarily localised. As time progresses one site of anodic attack initiates on the base substrate (circled on Figure 8B) and with further time, Figures 8C-8F, there is evidence of several rings of corrosion product emanating outward to the base metal either side of the weld zone. The morphology of attack is entirely consistent with the SVET results for the HSLA-HSLA welded couples as presented in 3.3 where focal anodic attack of the weld zone dominated the experiment with net cathodic activity detected on the base substrate.

In the case of welded HT UHSS- HT UHSS, as shown in Figures 9A-F, taken at 2 minute intervals, initiation of the anodic attack is not confined to the weld area with point anodic features developing on the base metal as circled in Figures 9B and 9C. However, a number of anodic sites develop within the weld and HAZ zones in Figure 9C and then persist through the experiment, leading to general darkening of these and the development of significantly localised points of anodic attack. It would seem, however, that the anodic sites initiate preferentially away from the central point of the weld zone, towards the boundary of the weld zone and the HAZ, and within the HAZ itself. Once again these data are consistent with that of the SVET for the HT UHSS-HT UHSS welded couple where the edges of the weld zone were observed to undergo preferential attack with anodes also observed to initiate on the base substrate away from the weld zone.

In the case that the HSLA steel grade is laser welded to the HT UHSS, as shown in Figures 10 A-F taken, initiation of anodes occurs exclusively on the HT UHSS associated with the periphery of the weld zone, and also on the base substrate (circled in Figure 10C). The anodes that form once again display the morphology of localised attack. No anodes initiate

on the HSLA steel throughout the duration of the experiment and the surface of the HSLA part of the coupled sample appears unchanged throughout. This fully supports the SVET results for the HSLA-HT UHSS welded couple where preferential attack of the HT UHSS was initially observed at the periphery of the weld zone with progression onto the base substrate.

(Figure 8)

(Figure 9)

(Figure 10)

4. Discussion

In the case that each steel sample is welded to a sample of the same grade corrosion primarily occurs within the welded zone, this being demonstrated by both SVET, where the red anodic regions correlate with the position of the weld, and by time lapse microscopy, which shows the formation of corrosion product in the weld zone and adjacent HAZ. For the HSLA-HSLA welded sample this focal attack at the weld is likely due to the formation of martensite within the welded zone. Evidence of martensite in the weld zone (labelled in Figure 8) is shown in Figure 11 and has been demonstrated in previous research [31-32]. Martensite is generally less corrosion resistant than ferrite-pearlite microstructures due to its non-equilibrium structure and large grain boundary length per unit area [33]. An example of the lower nobility of this phase can be seen in Figure 3 for the UHSS grade where the shift in microstructure from the ferrite-pearlite to martensitic through heat treatment resulted in a lower open circuit potential of ca. 0.1 V vs. SHE for the initial hours of exposure in 0.017 M NaCl.

(Figure 11)

During laser welding of UHSS boron steels the fast cooling rate generally creates a hard and brittle martensitic structure in the weld metal and parts of the heat affected zone (HAZ) where the temperature has reached the upper part of the austenitisation area [34]. This behaviour is expected and previous work has shown the welded area of 22MnB5 to be less corrosion resistant than the base material [10-11]. It is of interest that for this welded couple, corrosion seemed to initiate readily in the area at the periphery of the weld zone bounding the HAZ. The reason for this is, as yet, unknown. However, it has previously been shown that the mechanical properties of this region are reduced in terms of hardness due to the region experiencing temperatures only slightly exceeding the austenisation temperature, and therefore undergoing incomplete austenisation [35]. On cooling, areas of ferrite and carbide form that affect the mechanical properties [35]. It is also possible that electrochemical properties of this region are affected, locally, through the creation of galvanic cells between the ferrite containing regions and the surrounding martensite. Subsequently, given the difference in OCP between the AR (ferrite-pearlite) and HT (martensitic) UHSS shown in Figure 3, corrosion would initiate primarily in this area.

In comparison, in the case that the HSLA steel is laser welded to HT UHSS the anodic activity is initially focused on the weld/ HAZ on the UHSS side of the couple but rapidly spreads across the HT UHSS sample, this being demonstrated by both the SVET (Figure 7) and time-lapse microscopy (Figure 10). At the end of each experiment the HSLA substrate remains corrosion free. This behavior is indicative of formation of a galvanic cell between the two steel grades with the HT UHSS being anodically attacked and the HSLA being protected through cathodic polarisation. This galvanic cell is further evidenced by the open circuit potential and ZRA data shown in Figure 3 and Figure 4. The anodic

behavior of the HT UHSS with respect to the HSLA is best explained on the basis of the initial difference in OCP existing between the two metals as demonstrated in Figure 3, which shows the OCP of the HT UHSS to be ca. 0.2 V vs. SHE lower than that for the HSLA steel sample. Once the locations of the net anodic and net cathodic activity become physically separated this OCP difference will rapidly become amplified through differentiation of solution pH. The magnitude and polarity of the local current density values observed in the SVET experiments can be understood in terms of the local passivation and de passivation of the steel surfaces [36]. Thus the HSLA forms a strong cathode, and the HT UHSS is strongly anodic due to the initial differences in their OCP. Once established, this cell polarity will be maintained and reinforced by the local activation of the cathodic electrolyte through reaction (3) and acidification of the anodic electrolyte though reaction (4) and (5).

$$O_2 + 2H_2O + 4e^- \rightarrow 4OH^- \quad (3)$$

$$Fe \rightarrow Fe^{2+} + 2e^- \quad (4)$$

$$Fe^{2+} + 2H_2O \rightarrow Fe(OH)_2 + 2H^+ \quad (5)$$

The initial difference in OCP between the two materials is believed to be caused by two phenomena, firstly deviations in chemical composition (shown in Table 1 and 2) and secondly differences in microstructures, phase size and distribution. Fully martensitic microstructures have a high residual strain energy and a large surface area due to the diffusionless formation of a body centred tetragonal (BCT) structure from austenite [33]. As mentioned previously an initial potential difference of ca. 0.1 V vs. SHE was observed in the first 2 hours of exposure to 0.017 M NaCl for martensitic UHSS compared to as received ferrite-pearlite microstructures as shown in Figure 3. The effect of material chemistry is more difficult to assess due to the range of elemental differences between the

two samples and thus an overall comparison of the effects of coupling these two grades is only possible through this investigation.

Localised corrosion, of the type shown in Figures 8-10, may lead to perforation or initiate crack formation and is therefore an issue for structural reliability, this being especially true in the case of down gauged material. The galvanic corrosion observed in the case that HSLA steel is welded to HT UHSS is therefore of practical significance.

5. Conclusions

An optical and electrochemical study has been completed in 0.017 M NaCl to investigate the galvanic corrosion of a HSLA steel grade, typically used during the production of automotive components, laser welded to an UHSS hot stamped boron grade. When samples of the same grade were laser welded together corrosion activity was focused on the weld zone, this being attributed to microstructural changes that had occurred during the welding process. In comparison, when HSLA was welded to HT UHSS anodic attack was located solely on the UHSS grade and exhibited a localised corrosion morphology. SVET derived mass loss was substantially higher in the case that dissimilar materials were welded when compared to the case for which samples of the same grade had been welded to one another.

5. Acknowledgments

The authors would like to thank Tata Steel UK for providing samples, EPSRC for funding via the MATTER Engineering Doctorate IDC (EP/I015507/1), and the College of Engineering (Swansea University) for their support.

References

1. United Nations, Kyoto Protocol to the United Nations Framework Convention on Climate Change, 1998.

2. Regulation (EU) No 333/2014 of the European Parliament and of the Council of 11 March 2014 amending Regulation (EC) No 443/2009 to define the modalities for reaching the 2020 target to reduce CO 2 emissions from new passenger cars.

3. K. Seto, Y. Funakawa, S. Kaneko, Hot rolled high strength steels for suspension and chassis parts 'NANOHITEN and 'BHT® steel", JFE Tech. Rep. 10 (2007) 19–25.

4. International Molybdenum Association, Molybdenum in Transportation; Car Body Chassis Suspension. Available at http://www.imoa.info/download_files/sustainability/IMOA_CarBody_Chassis_Construction.pdf. Last accessed 17th November 2017.

5. K. Olsson, J.-O. Sperle, New advanced ultra-high strength steels for the automotive industry, Auto Technology. 6 (2006) 46-49.

6. A. Mayyas, A. Qattawi, M. Omar, D. Shan, Design for sustainability in automotive industry: A comprehensive review, Renewable and Sustainable Energy Reviews. 16 (2012) 1845-1862.

7. O. Bouaziz, H. Zurob, M. Huang, Driving Force and Logic of Development of Advanced High Strength Steels for Automotive Applications, Steel Research International. 84 (2013) 937-947.

8. K. Dilger and S. Kreling, 9 - Adhesive bonding techniques for advanced high-strength steels (AHSS), in: M. Shome, M. Tumuluru (Eds.), Welding and Joining of Advanced High Strength Steels (AHSS), Woodhead Publishing, 2015 pp. 167-179.

9. G. Cole, Automotive Chassis/Suspension Materials, in: K.H.J. Buschow, R. W. Cahn, M. C. Flemings, B. Ilschner, E. J. Kramer, S. Mahajan, P. Veyssière (Eds.), Encyclopedia of Materials: Science and Technology, 2nd Edition, Pergamon, 2001.

10. D. Liu, H. Zhao, D. Tang, Q. Ma, Corrosion Behavior Study of 22MnB5 Steel and its Weld Using Electrochemical Method, Applied Mechanics and Materials. 496-500 (2014) 340-343.

11. A. M. El-Aziz, W. Sharaf, J. Drechsel, H. Exner, Mechanical and corrosion behaviour of hot stamped 22MnB5/ Usibor 1500 steel alloy Yb: YAG continuous fiber laser weldments, Ochrona przed Korozja. 7 (2014) 242.

12. K.-M. Hong, Y. C. Shin, Prospects of laser welding technology in the automotive industry: A review, Journal of Materials Processing Technology. 245 (2017) 46-69.

13. R. Kuziak, R. Kawalla, S. Waengler, Advanced high strength steels for automotive industry, Archives of Civil and Mechanical Engineering. 8 (2008) 103-117.

14. T.V. Philip, T. J. McCaffy, Ultrahigh Strength Steel, ASM Metals Handbook, 10th Edition, ASM International, Ohio, 1990.

15. J. R. Davis, High-Strength Low-Alloy Steels in Alloying: Understanding the Basics, ASM International, Ohio, 2001.

16. M. S. Rashid, High-strength low-alloy steels, Science. 208 (1980) 862.

17. C. I. Garcia, High strength low alloyed (HSLA) steels, in: R. Rana and S. B. Singh (Eds.), Automotive Steels; Design, Metallurgy, Processing and Applications, Woodhead Publishing, 2007, pp. 145-167.

18. N. Hägele, N., C. M. Sonsino, Structural durability of forged automotive aluminium chassis components submitted to spectrum loading and salt-corrosion by the example of a tension strut, Procedia Engineering. 10 (2011) 330–339.

19. G. Williams, H. N. McMurray, Localized Corrosion of Magnesium in Chloride-Containing Electrolyte Studied by a Scanning Vibrating Electrode Technique, Journal of the Electrochemical Society. 155 (2008) C340-C349.

20. M. Simões, A.C. Bastos, M.G. Ferreira, Y. González-García, S. González, R.M. Souto, Use of SVET and SECM to study the galvanic corrosion of an iron–zinc cell, Corrosion Science. 49 (2007) 726-739.

21. J. Elvins, J. A. Spittle, J. H. Sullivan, D. A. Worsley, The effect of magnesium additions on the microstructure and cut edge corrosion resistance of zinc aluminium alloy galvanised steel, Corrosion Science. 50 (2008) 1650-1658.

22. J. Sullivan, C. Weirman, J. Kennedy, D. J. Penney, Influence of steel gauge on the microstructure and corrosion performance of zinc alloy coated steels, Corrosion Science. 52 (2010) 1853-1862.

23. D. J. Penney, J. H. Sullivan, D. A. Worsley, Investigation into the effects of metallic coating thickness on the corrosion properties of Zn–Al alloy galvanising coatings, Corrosion Science. 49 (2007) 1321-1339.

24. D. Mun, E. Shin, Y. Choi, J. Lee, Y.Koo, Effects of cooling rate, austenitizing temperature and austenite deformation on the transformation behavior of high strength boron steel, Materials Science and Engineering A. 545 (2012) 214-224.

25. S. Bohm, H.N. McMurray, S.M. Powell, D.A. Worsley, Photoelectrochemical investigation of corrosion using scanning electrochemical techniques, Electrochimica Acta. 45 (2000) 2165-2174.

26. D. Worsley, H. N. McMurray, A. Belghazi, Determination of localised corrosion mechanisms using a scanning vibrating reference electrode technique, Chem. Commun. 24 (1997) 2369-2370.

27. G.W.C. Kaye, T.H. Laby, Tables of Physical and Chemical Constants, Longman, London, 1986.

28. D.A. Worsley, H.N. McMurray, J.H. Sullivan, I.P. Williams, Quantitative Assessment of Localized Corrosion Occurring on Galvanized Steel Samples Using the Scanning Vibrating Electrode Technique, Corrosion. 60 (2004) 437-447.

29. J. H. Sullivan, S. Mehraban, J. Elvins, In situ monitoring of the microstructural corrosion mechanisms of zinc–magnesium–aluminium alloys using time lapse microscopy, Corrosion Science. 53 (2011) 2208-2215.

30. J. Sullivan, N. Cooze, C. Gallagher, T. Lewis, T. Prosek, D. Thierry, In situ monitoring of corrosion mechanisms and phosphate inhibitor surface deposition during corrosion of zinc–magnesium–aluminium (ZMA) alloys using novel time-lapse microscopy, Faraday Discussions. 180 (2015) 361-379.

31. R. Oyyaravelu, P. Kuppan, N. Arivazhagan, Metallurgical and mechanical properties of laser welded high strength low alloy steel, Journal of Advanced Research. 7 (2016) 463-472.

32. A. Santillan Esquivel, S. S. Nayak, M. S. Xia1, Y. Zhou, Microstructure, hardness and tensile properties of fusion zone in laser welding of advanced high strength steels, Canadian Metallurgical Quarterly. 51 (2012) 328-335.

33. H.K.D.H. Bhadeshia and R. Honeycombe, 5 - Formation of Martensite, in: Steels (Third Edition), Butterworth-Heinemann, Oxford, 2006, pp. 95-128.

34. N. Farabi, D. L. Chen, J. Li, Y. Zhou, S. J. Dong, Microstructure and mechanical properties of laser welded DP600 steel joints, Materials Science and Engineering: A. 527 (2010) 1215-1222.

35. N. Farabi, D. L. Chen, Y. Zhou, Microstructure and mechanical properties of laser welded dissimilar DP600/DP980 dual-phase steel joints, Journal of Alloys and Compounds. 509 (2011) 982-989.

36. A.deS. Brasunas, N. E. Hamner, NACE Basic Corrosion Course, NACE, Texas, 1970.

7. Figure Legends

Figure 1. A schematic diagram of the experimental setup used for the time lapse photography of welded samples.

Figure 2. a.) An optical image of the HSLA steel surface b.) An optical and SEM image of UHSS surface.

Figure 3. Free Corrosion Potential of HSLA and UHSS grades in 0.017 M NaCl (aq) electrolyte. **To show the reproducibility three measurements are shown for each material.**

Figure 4. The net galvanic current density, as measured by a zero resistance ammeter at open circuit potential, flowing from a heat treated UHSS sample to a HSLA sample recorded as a function of time in 0.017 M NaCl (aq) electrolyte. A positive current indicates that the HT UHSS is acting anodically. To show the reproducibility three measurements are shown.

Figure 5. SVET derived surface plots maps showing the distribution of normal current density i_z above a laser welded HSLA-HSLA steel sample freely corroding in 0.017 M NaCl (aq) electrolyte after various times of immersion, and an image of the sample post immersion.

Figure 6. SVET derived surface plots maps showing the distribution of normal current density i_z above a laser welded heat treated UHSS-UHSS steel sample freely corroding in 0.017 M NaCl (aq) electrolyte after various times of immersion, and an image of the sample post immersion. Localised anodic features observed on base substrate are circled.

Figure 7. SVET derived surface plots maps showing the distribution of normal current density i_z above a HSLA steel sample welded to a heat treated UHSS sample, freely corroding in 0.017 M NaCl (aq) electrolyte after various times of immersion, and an image of the sample post immersion.

Figure 8. Optical microscope images of laser welded HSLA steel taken in situ under immersion conditions in NaCl (aq) electrolyte. Images shown were taken at two minute intervals. Site of anodic attack on base substrate circled.

Figure 9. Optical microscope images of a laser welded heat treated UHSS sample taken in situ under immersion conditions in NaCl (aq) electrolyte. Images shown were taken at two minute intervals. Sites of localised anodic attack circled.

Figure 10. Optical microscope images of a HSLA grade steel sample laser welded to heat treated UHSS taken in situ under immersion conditions in NaCl (aq) electrolyte. Images shown were taken at two minute intervals. Sites of localised anodic attack circled.

Figure 11. Optical microscope images of the weld zone of a laser welded HSLA-HSLA grade steel sample.

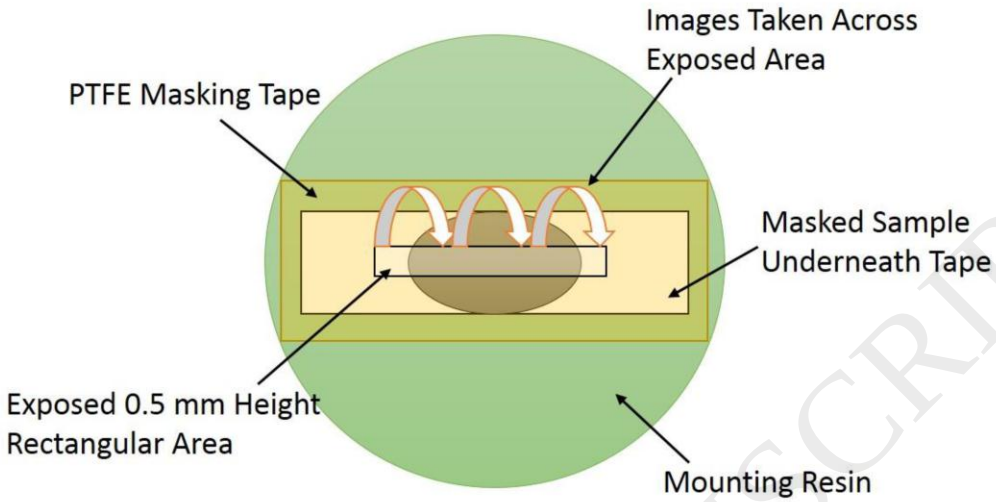

Figure 1

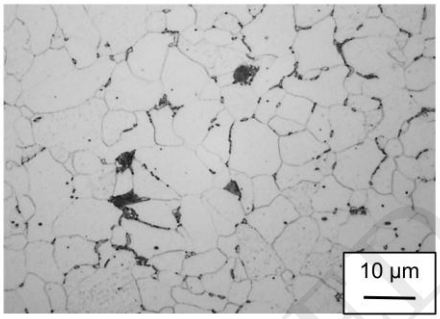

a.)

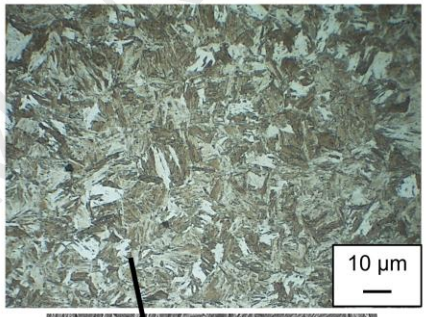

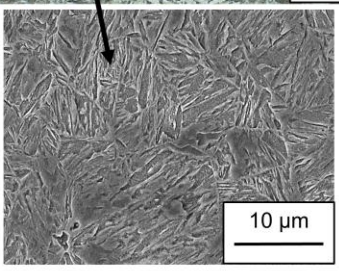

b.)

Figure 2

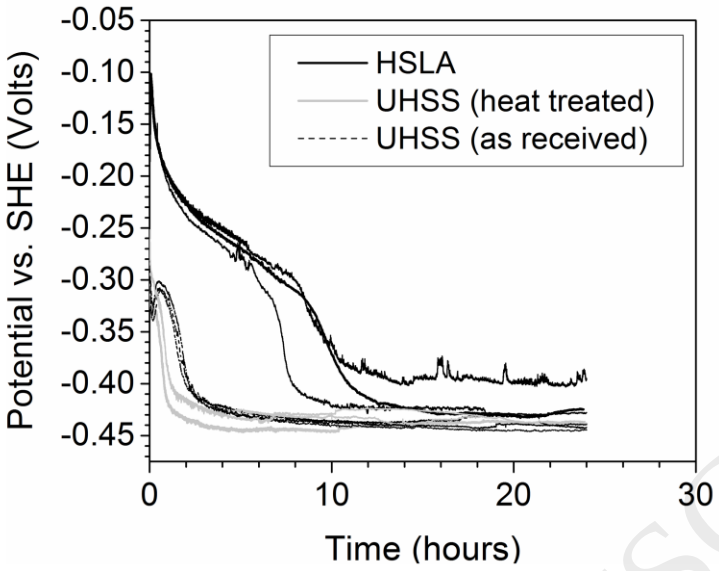

Figure 3

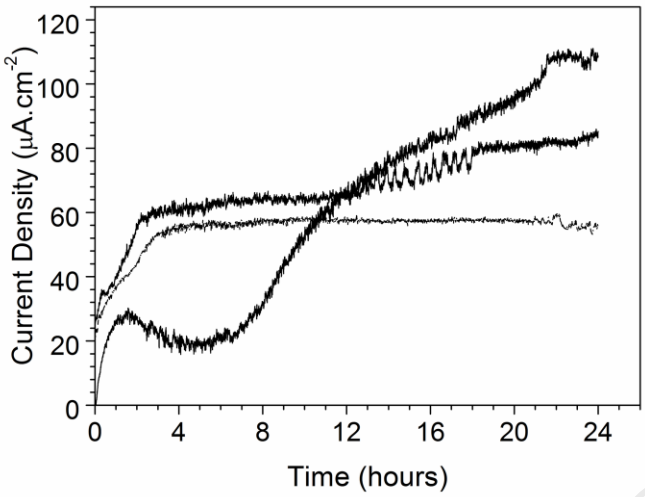

Figure 4

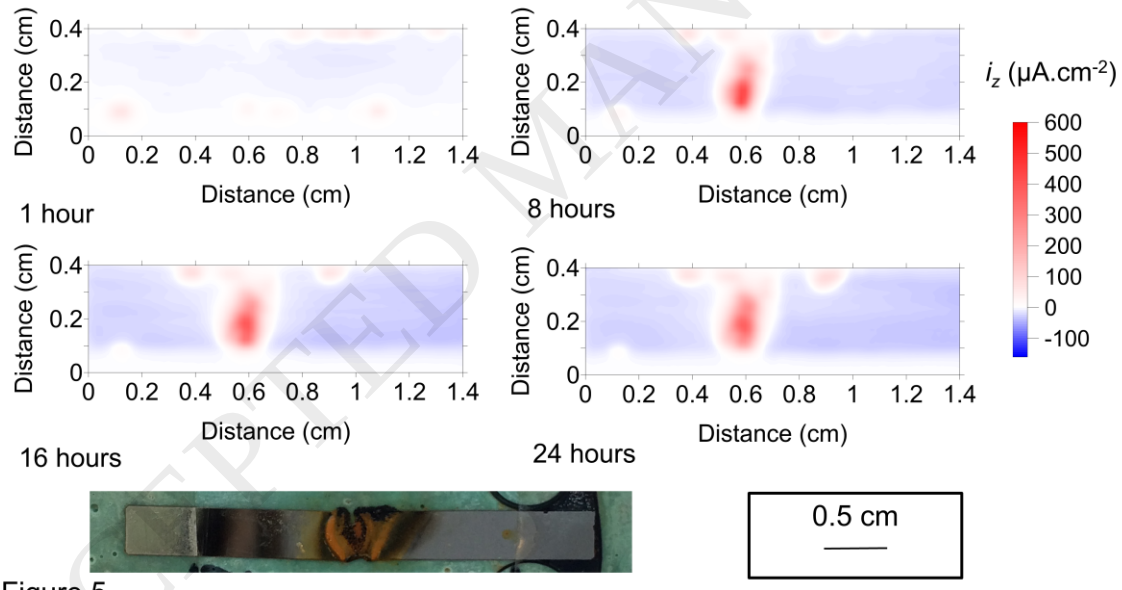

Figure 5

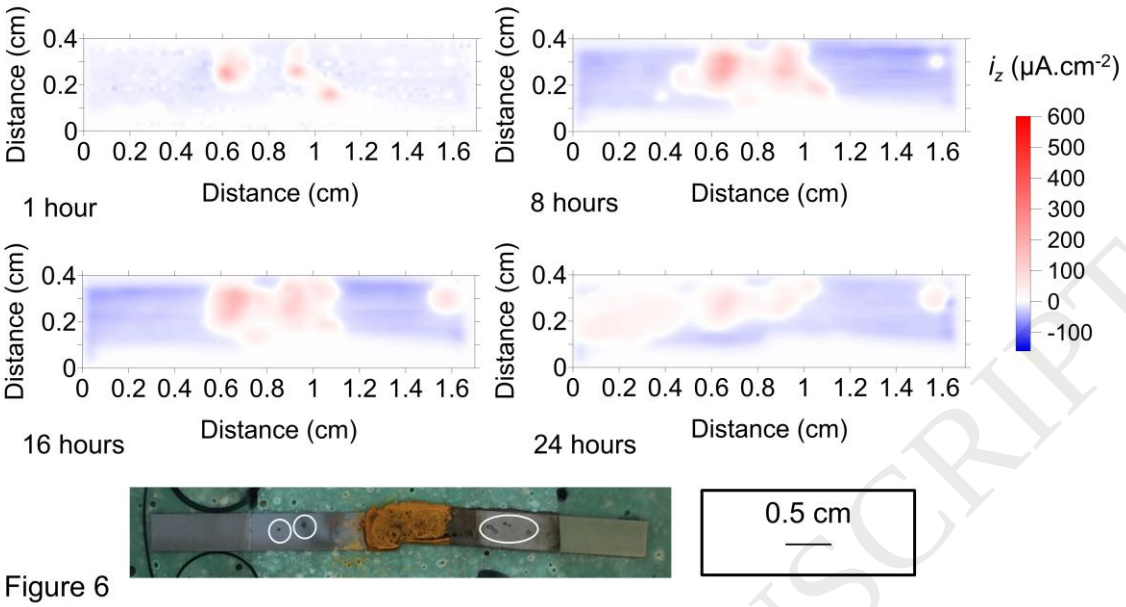

Figure 6

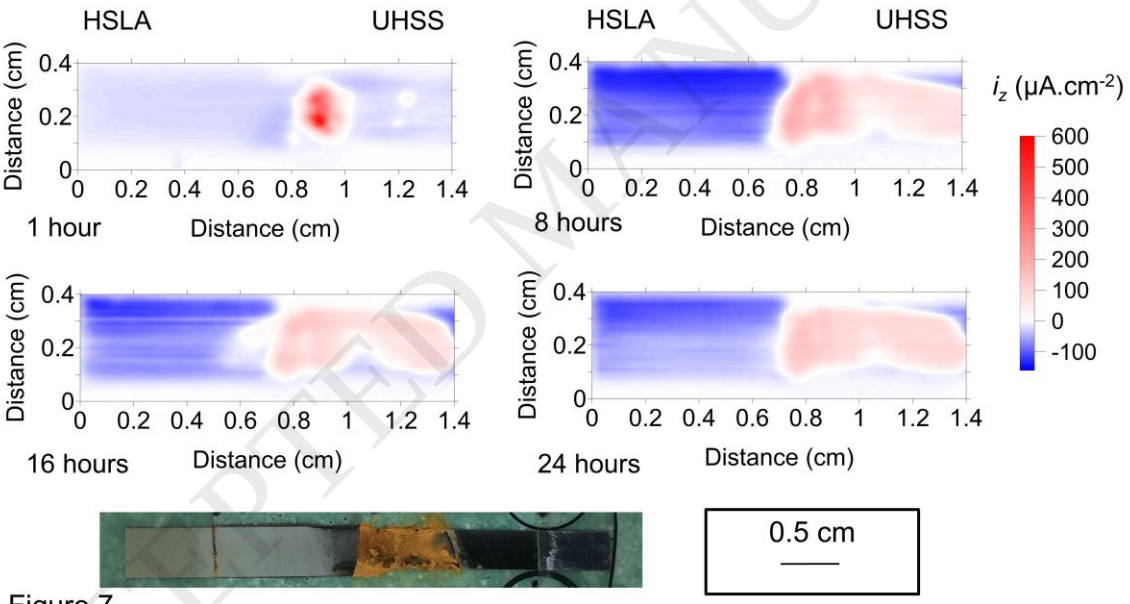

Figure 7

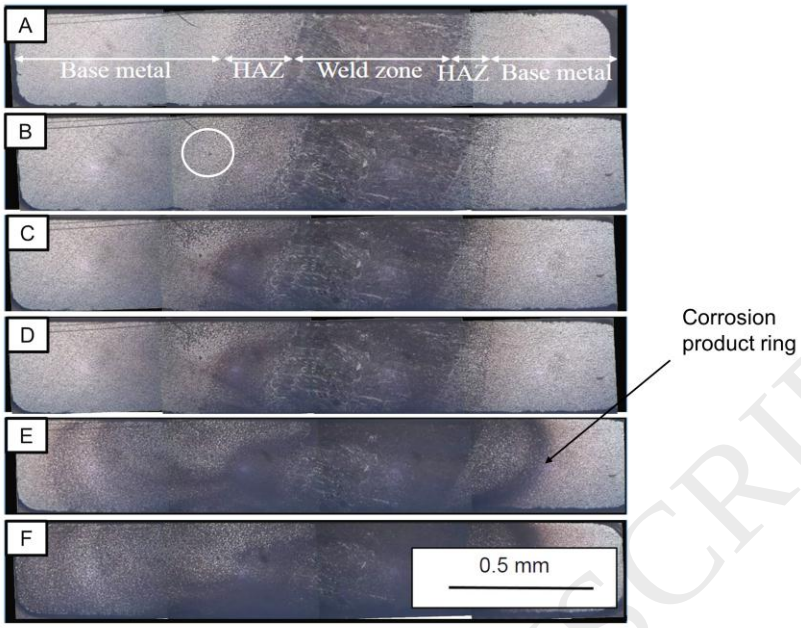

Figure 8

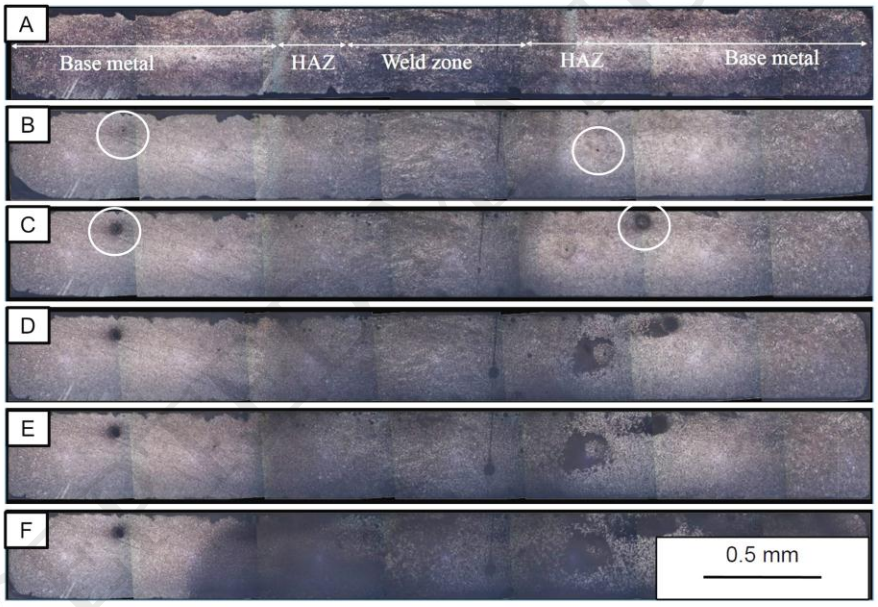

Figure 9

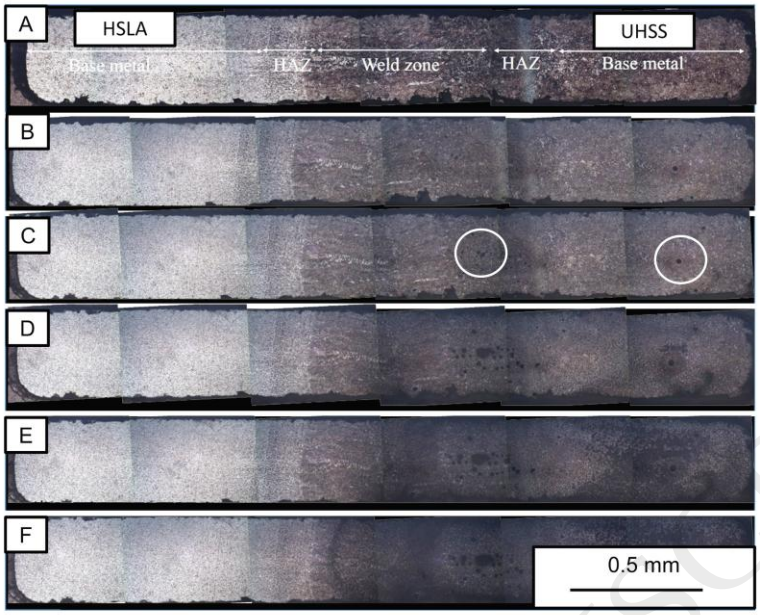

Figure 10

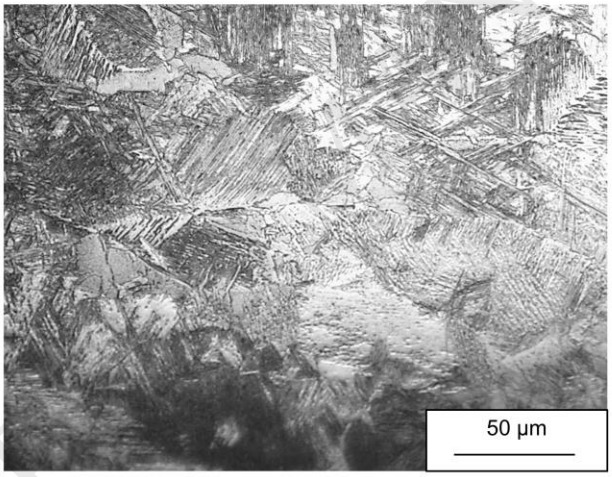

Figure 11

8. Tables

Table 1. The chemical composition of the HSLA steel. Values provided in weight percentages.

C	Si	Mn	P	S	Al	Nb
0.069	0.015	0.495	0.019	0.005	0.029	0.022

Table 2. The chemical composition of the UHSS grade steel. Values provided in weight percentages.

C	Si	Mn	P	S	Al	Cr	Ti	B
0.25	0.279	1.223	0.02	0.0015	0.041	0.145	0.033	0.0029

Table 3. SVET derived mass loss calculated for welded steel samples freely corroding in 0.017 M NaCl (aq) electrolyte for 24 hours.

Sample	Mass loss (µg.cm^{-2})
HSLA-HSLA	241 ± 24
Heat treated UHSS-UHSS	197 ± 12
HSLA-UHSS	505 ± 19